MATERIALS CHEMISTRY FRONTIERS

RESEARCH ARTICLE

View Article Online
View Journal

Cite this: DOI: 10.1039/d5qm00765h

Toroidal ferroelectric cobalt-doped barium titanates as efficient energy conversion materials for solar cells and photocatalysis

Murali Balu,[a] Duraisamy Kumaresan,*[ab] R. Krishna Prasad[ab] and Subhash Kalidindi[c]

Doughnut-shaped ferroelectric barium titanate (BTDS) and cobalt-doped barium titanate (CBTDS) [$Co_xBaTi_{1-x}O_3$ (x = 0 or 0.05 mol%)] nanostructures have been synthesized from hydrogen titanate nanowires for use as efficient photon energy conversion materials in dye-sensitized solar cells (DSSCs) and photocatalytic dye degradation applications. The morphological and structural analyses have revealed that the perovskite BDTS and CBDTS nanostructures exhibit toroidal ferroelectric characteristics, which are reinforced by the formation of oxygen vacancies and Ti^{3+} ions within their lattices. The DSSC bilayer photoanodes constructed using mesoporous TiO_2 nanoparticles (TNP) as the underlayer and CBTDS as the light-scattering and charge-collecting upper layer have shown the highest photovoltaic efficiency of 10.29 ± 0.44% due to the greater light scattering, light absorption extended to the near-infrared region, and toroidal ferroelectric field-induced slower charge recombination effects that collectively boosted the photovoltaic performance. Moreover, the photocatalytic dye-degradation performance of the CBTDS photocatalyst has demonstrated a maximum dye degradation efficiency of 86.74% over 75 minutes, indicating a respectable photocatalytic activity compared to the BTDS photocatalyst. These results have confirmed that superior morphology control, oxygen vacancy, and Ti^{3+} ion formation in the BTDS and CBTDS nanostructures strongly influence toroidal ferroelectric field-induced charge separation and light-harvesting ability in dye-sensitized solar cells (DSSCs) and photocatalysts, leading to superior performance.

Received 20th January 2026,
Accepted 24th March 2026

DOI: 10.1039/d5qm00765h

rsc.li/frontiers-materials

Introduction

Barium titanate ($BaTiO_3$), a prominent perovskite, is a multifunctional inorganic material with versatile electric (high k-dielectric, piezoelectric, ferroelectric, *etc.*) and electrooptic properties, establishing it as a promising component for many technological applications such as data storage,[1,2] energy conversion,[3] nanogenerators,[4] sensors,[4,5] memory devices,[5] catalysis,[6] photonics and multilayer ceramic capacitors,[7] and solar cells.[8] Characteristically, in many of these device applications, various multi-dimensional $BaTiO_3$ nanostructures, such as nanocubes,[9] nanorods,[10] nanowires,[11] hybrid nanotubes,[12] and nanodisks,[13] that have been employed with preferred optical, electronic, and dielectric properties prepared controllably by the solvothermal, hydrothermal, electrospinning, and molten-salt synthesis methods are well known in the literature. Also, several multi-dimensional inorganic perovskite ABO_3 (A = Ba, Sr, Ca, and Mg; B = Ti) nanostructures prepared by using the hydrothermal process from precursor materials like MCl_2 as a metal source (M) and titanium dioxide as a Ti-reactant, which in turn supported tuning the electro-optical properties of their perovskite nanostructures, are familiar.[5] Recently, well-aligned $BaTiO_3$ nanorods hydrothermally prepared onto conducting substrates functioning as efficient nanocomposite energy harvesters have been investigated for self-powered applications.[4] Also, the enhanced light-harvesting ability of the hierarchical $BaTiO_3$ nanorod flowers in the dye-sensitized solar cell (DSSC) photoelectrode has produced the highest power conversion efficiency (PCE) of 4.14%.[14] Our group has demonstrated that the ferroelectric barium titanate nanorod microspheres, prepared *via* a two-step hydrothermal technique, can be used in flexible polymer photoelectrodes to produce flexible polymer DSSCs and photodetectors with superior performance.[15] Liu and coworkers have investigated the pyroelectric synthesis of Au–$BaTiO_3$ hybrid NPs to enhance performance in dye degradation by efficiently

[a] *Solar Energy and Optoelectronics Research Laboratory, COE-AMGT, Amrita School of Engineering, Amrita Vishwa Vidyapeetham, Coimbatore, 641112, India. E-mail: k_duraisamy@cb.amrita.edu*
[b] *Department of Chemical Engineering and Materials Science, Amrita School of Engineering, Amrita Vishwa Vidyapeetham, Coimbatore, India*
[c] *Department of Chemical and Biological Engineering, Tufts University, Medford, Massachusetts, 02155, USA*

harvesting thermal energy in the pyro-catalysis process.[16] In addition, magnetoelectric and ferroelectric coupling in $CoBaTiO_3$ ceramics with a tetragonal crystal structure, showing an unusual coupling between magnetic parameters useful for applications such as memory storage, spintronics, and other multifunctional electronic/magnetic devices, has been reported by Pradhan *et al.*[17]

Furthermore, Co-doped $BaTiO_3$ multiferroic ceramic materials, such as $BaTi_{1-x}Co_xO_3$ (BTCO) ceramics, have been investigated for producing excellent magnetic, structural, electrical, and magnetoelectric properties.[18,19] Several metal-doped $BaTiO_3$ multiferroic nanocrystals (M = Cr, Mn, Fe, Co) are demonstrated as suitable materials for superior energy conversion and data storage applications.[20] It has been proven that Cr, Mn, Fe, Nb, and Co are exceptional dopants for Ba and Ti in the $BaTiO_3$ lattice to instigate a ferromagnetic and ferroelectric property.[21,22] Due to this, room-temperature ferroelectric and multiferroic characteristics have been observed in Co- or Nb-doped Ba(Sr, Ti)O_3 thin films.[23,24] Besides, frequency-dependent dielectric properties of cobalt-doped $BaTiO_3$ and their graphene nanoplatelet (GNP) composites have been investigated for energy storage applications.[25] In addition, one-dimensional barium titanate nanowires and their GNP composites in various weight proportions synthesized *via* a hydrothermal process and utilized as light-scattering layers of the bilayer photoanodes to fabricate high-performance DSSCs have been reported recently by our group.[26] Similarly, ferroelectric two-dimensional $BaTiO_3$-based planar-structured and vertical-structured photoactive materials have been studied for enhanced photocurrent generation in photovoltaic and photodetector applications.[27,28] Nevertheless, reports available on toroid- or doughnut-shaped ferroelectric barium titanate (BTDS) and Co-doped barium titanate (CBTDS) nanostructures investigated as the superior solar energy harvesting materials in DSSC and photocatalysis applications to date are scarce. Thus, in this work, doughnut-shaped barium titanate (BTDS) and Co-doped barium titanate (CBTDS) nanostructures as the light scattering and absorbing layer of the bilayer photoelectrodes (TNP + BTDS and TNP + CBTDS), using a common TiO_2 nanoparticle (TNP) underlayer, are investigated for improving the photovoltaic performance of DSSCs to an impressive PCE of more than 10%.

Moreover, the photocatalytic activity of the tetragonal and cubic phases of $BaTiO_3$ in decolorizing Rhodamine B dye has been investigated under one-sun illumination, and a threefold rise in the decolorization rate by the ferroelectric tetragonal phase over the cubic phase has been proven.[29] The influence of ferroelectricity on dye molecules is the separation of photoexcited carriers due to the internal space charge layer favored by the ferroelectric dipoles, which enhances photocatalytic degradation faster. Also, textured $BaTiO_3$ nanorod arrays synthesized *via* the hydrothermal method for piezo-catalytic degradation of Rhodamine B with a dye removal efficiency of more than 97% have been reported recently.[30] So, this work compares the rhodamine B dye degradation efficiency of the BTDS and CBTDS photocatalysts to analyze the photocatalytic activity, along with the DSSC photocurrent responses to demonstrate them as highly versatile, efficient, and multi-functional photoactive nanostructures for use in high-performance solar energy conversion applications.

Experimental

Synthesis of $H_2Ti_2O_5{\cdot}H_2O$ nanowires (HTNWs)

1 g of titanium dioxide nanopowder was added to 60 mL of aqueous 10 M NaOH solution and then transferred to a 100 mL Teflon-lined hydrothermal acid digester. Subsequently, the sealed acid digester was heated in a muffle furnace at 160 °C for 24 h and cooled to room temperature. Products formed in the acid digester were neutralized with 0.1 M HCl, washed several times in deionized water and ethanol, and dried at 80 °C for 12 h. The wet products formed were then calcined at 500 °C for 2 h in a silica crucible and cooled to room temperature to obtain the $H_2Ti_2O_5{\cdot}H_2O$ nanowires (HTNW) powder.

Synthesis of $BaTiO_3$ doughnut-shaped (BTDS) nanostructures

A mixture of 0.5 g of HTNW powder, 50 ml of deionized water, and 1 g of barium hydroxide octahydrate was transferred into a Teflon-lined hydrothermal acid digester and heat-treated in a muffle furnace at 120 °C for 6 h. Then, the acid digester was cooled to precipitate out the barium titanate solids, then washed with deionized water and ethanol several times to form a wet product. The wet product was warmed at 80 °C in an oven for 12 h, subsequently cooled to obtain the dry doughnut-shaped barium titanate powder. Afterward, the dry powder was calcined at 500 °C for 2 h in a silica crucible and then cooled to get the pure product.

Synthesis of $CoBaTiO_3$ doughnut-shaped (CBTDS) nanostructures

0.5 g of BTDS powder, 60 mL of deionized water, and 0.65 g of $CoCl_2{\cdot}6H_2O$ mixture were added to a Teflon-lined hydrothermal acid digester and heated to 120 °C for 85 minutes. Later, the acid digester was cooled to obtain the cobalt-doped barium titanate as green sediment. The sediment was stirred, filtered, and washed abundantly with deionized water and ethanol to produce doughnut-shaped cobalt-doped barium titanate as a pale green product without impurities. This product was heated to 80 °C for 6 h to obtain its dry powder. The dry powder product was further calcined at 500 °C for 2 h in a crucible and then cooled to form the pure product by the sequence of steps shown in Scheme 1, through the chemical reactions shown in Scheme S1, and the pure products were made as scattering layer pastes using a literature procedure[8] [SI].

Fabrication of DSSCs using BDTS and CBDTS nanostructure photoanodes

Two bilayer DSSC photoelectrodes, namely TNP + BTDS and TNP + CBTDS, are fabricated using their scattering layer pastes and TiO_2 nanoparticle (TNP) paste prepared from their respective powder samples (SI). Briefly, the TNP viscous paste layer was coated using the doctor blading method onto the pre-cleaned

Scheme 1 Schematic of the steps involved in forming $H_2Ti_2O_5{\cdot}H_2O$ nanowires and $BaTiO_3$ and $CoBaTiO_3$ doughnut nanostructures.

FTO conducting glass (0.4 × 0.4 cm^2 dimension) substrates. Subsequently, the TNP-coated FTO substrates were dried in air for 30 min and then annealed using a muffle furnace at 150 °C for 30 min and 480 °C for 30 min, and then cooled to room temperature. In the second step, the CBTDS and BTDS light-scattering layer pastes were individually deposited on top of each TNP underlayer deposited on the FTO substrate by the doctor blading method using a Scotch tape enclosure made of two sheets to obtain a bilayer cell active area of 0.16 cm^2 dimension and air-dried for 30 min. After that, each TNP + BTDS and TNP + CBTDS bilayer-coated FTO glass substrate was annealed successively at 150 °C for 30 min and 500 °C for 30 min, and cooled to 80 °C. Then, each substrate was soaked for 12 h in a 0.1 mM N719 ethanol dye solution to obtain its respective bilayer DSSC photoanode. The DSSC counter electrodes were prepared by coating 0.05 mol L^{-1} of H_2PtCl_6 isopropyl alcohol solution onto the FTO *via* a solution-casting method and then annealed at 400 °C for 30 min. The DSSCs were constructed individually as sandwich-type cells using respective bilayer photoanodes, counter electrodes, and Surlyn™ ionomer polymer masks. Finally, 0.5 M LiI + 0.05 M I_2 + 0.5 M 4-*tert*-butyl pyridine redox electrolyte solution was injected into the sandwich cell arrangement to obtain the functioning DSSCs.

Results and discussion

Crystal structure and phase identification

The BTDS and CBTDS nanostructures are successfully prepared by using the HTNW precursor *via* a multi-step hydrothermal digestion process shown in Scheme 1. The as-prepared HTNWs' XRD pattern [Fig. S1, SI] indicates that the precursor anatase TiO_2 nanoparticles are transforming into a less symmetric, orthorhombic titanate nanowire. Also, the intense diffraction peaks observed at 2θ angles of 9.58°, 24.68°, 29.48°, 48.68°, and 62.68° for the planes (200), (110), (310), (020), and (002), respectively, confirm an orthorhombic unit cell (JCPDS-47-0124).[31–33] Several strong peaks observed at 2θ angles of 9.58°, 24.68°, and 29.48° are attributed to the diffraction of the layered titanate structure and assigned to $X_2Ti_3O_7$ or $X_2Ti_2O_5{\cdot}H_2O$, where X = Na and H, and lepidocrocite-type titanate with peak broadening as shown in Fig. S1 (SI). Upon the addition of HCl to $Na_2Ti_2O_5{\cdot}H_2O$, the ratio of H/Na in the HTNW sample increases because the H^+ ion replaces the Na^+ ion in the orthorhombic crystal. When the HCl solution amount is increased to 100 mL, $Na_2Ti_2O_5{\cdot}H_2O$ is completely transformed into $H_2Ti_2O_5{\cdot}H_2O$, implying that the chemical composition of titanate nanowires strongly depends on the ion exchange process.[4] Also, the final product isolated is confirmed as $H_2Ti_2O_5{\cdot}H_2O$ layers of orthorhombic phase crystallites in the form of 1D nanowires.

Moreover, the XRD pattern of BTDS prepared from HTNWs displayed intense diffraction peaks at 2θ angles of 22.18°, 31.49°, 38.84°, 45.12°, 45.36°, 50.89°, 56.17°, 65.73°, 70.35°, 74.82° and 79.09°, corresponding to the Miller indices of (100), (110), (111), (200), (002) (210), (211), (220), (300), (310) and (311) planes, respectively, revealing a tetragonal phase crystal structure (JCPDS 05-0626),[24,34,35] as shown in Fig. 1(a). The tetragonal phase BTDS is formed by the transformation of an orthorhombic 1D nanowire structure into a 3D doughnut nanostructure during the second stage of the hydrothermal process. In addition, the CBTDS crystal structure is verified from the XRD pattern, as shown in Fig. 1(a). The diffraction pattern of CBTDS shows resemblance to its precursor BTDS by exhibiting a similar pattern without significant changes in the peak positions observed at 2θ angles of 22.16°, 31.45°, 38.80°, 45.09°, 45.34°, 50.86°, 56.14°, 65.70°, 70.33°, 74.79°, and 79.06° corresponding to the miller indices

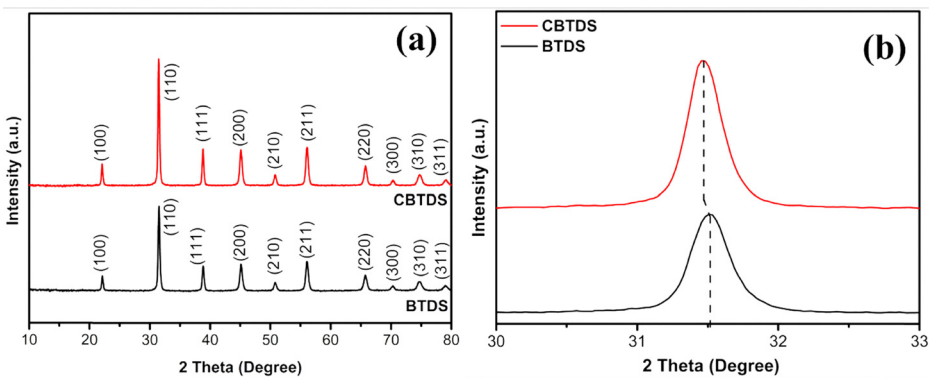

Fig. 1 (a) X-ray diffraction (XRD) patterns of BTDS and CBTDS nanostructures, (b) enlarged view of the diffraction peak angle from 30° to 33°.

of (100), (110), (111), (200), (002), (210), (211), (220), (300), (310), and (311) planes, respectively, of the tetragonal phase crystal structure (JCPDS 05-0626).[24,34,35] Besides, an enlarged view of the diffraction peak from 31° to 33° reveals that the peak at 31.4° corresponds to the (110) plane (Fig. 1b), a characteristic of the tetragonal crystal structure. Also, a slight shift in this diffraction peak position towards a lower value is observed. This shift strongly suggests the successful incorporation of the cobalt (Co) dopant into the tetragonal $BaTiO_3$ lattice. This can be attributed to the replacement of both Ba^{2+} and Ti^{4+} ions in the lattice by the Co^{2+} ions, leading to a minor lattice distortion that could cause the peak shift to the lower 2θ value, and a slight increase in the lattice parameters may be due to the formation of Ti^{3+} ions and oxygen vacancies in the lattice.[24,36] The crystallite sizes of BTDS and CBTDS nanostructures are calculated based on the peak full width at half maximum (FWHM) of the peak corresponding to the (110) plane by using Debye–Scherrer's equation.[37] The estimated crystallite sizes of BTDS and CBTDS nanostructures are listed in Table S2 [SI]. The XRD results indicated an increased crystallite size of 42 nm after incorporating the Co metal dopant into the bare BTDS, with a crystallite size of about 33.9 nm. The unit cell expands when Co^{2+} ions replace Ti^{4+} ions in the BTDS lattice, creating oxygen vacancies. The oxygen vacancies can significantly influence the electrical properties of the CBTDS ceramics compared to the BTDS. In general, with lower oxygen vacancies, crystallites remain in the tetragonal phase, and possibly increasing oxygen vacancies induce phase transformation from tetragonal into the hexagonal/cubic phase, which is widely proven in recent literature.[36] Further, the cobalt dopant concentration is directly linked to the oxygen vacancies formed in the CBTDS lattice; when the cobalt dopant concentration is >0.05 mol%, it can produce a noticeable change that is detected in the X-ray diffraction. In this study, Co-dopant concentration has been kept lower than 0.05 mol%; hence, the doping has not created any discernible phase transformation except the marginal rise in the crystallite size, as observed in Table S2 and Fig. 1.

Morphology transformation and control

The morphology of the as-prepared BTDS and CBTDS is shown in Fig. 2(a)–(d). To understand the 1-dimensional to 3-dimensional morphological transformation of the nanostructures, a detailed FESEM analysis has been performed for the precursor HTNWs and presented in Fig. S3(a) and (b) [SI]. Similarly, FESEM images of BTDS and CBTDS morphologies at different magnifications are shown in Fig. 2(a), (c) and (b), (d), respectively. The higher magnification FESEM images of BDTS and CBDTS (Fig. 2(a), (c) and (b), (d)) indicate that the nanostructures are formed as well-dispersed doughnut-shaped structures. Also, the FESEM analysis revealed that the as-prepared HTNWs, BTDS, and CBTDS formed predominantly as non-agglomerated nanostructures. The FESEM images in Fig. S3 confirm that the as-synthesized H-titanate nanowires are transformed from 0-dimensional (0D) anatase TiO_2 nanoparticles into 1-dimensional (1D) orthorhombic nanowires. According to the FESEM images in Fig. 2(a) and (c), the three-dimensional (3D) BTDS nanostructures have been successfully formed from the 1D orthorhombic HTNWs. The temperature effect on the $BaTiO_3$ morphology and size indicated that at 120 °C, hydrothermal treatment for 6 h produces a well-organized, mesoporous, tetragonal BTDS with narrow dispersity.[13] Besides, the 3D tetragonal BTDS nanostructures transformed into CBTDS without morphology change during the hydrothermal process, while using less than 0.05 mol% of Co^{2+} dopant concentration, causing minimal lattice distortion.

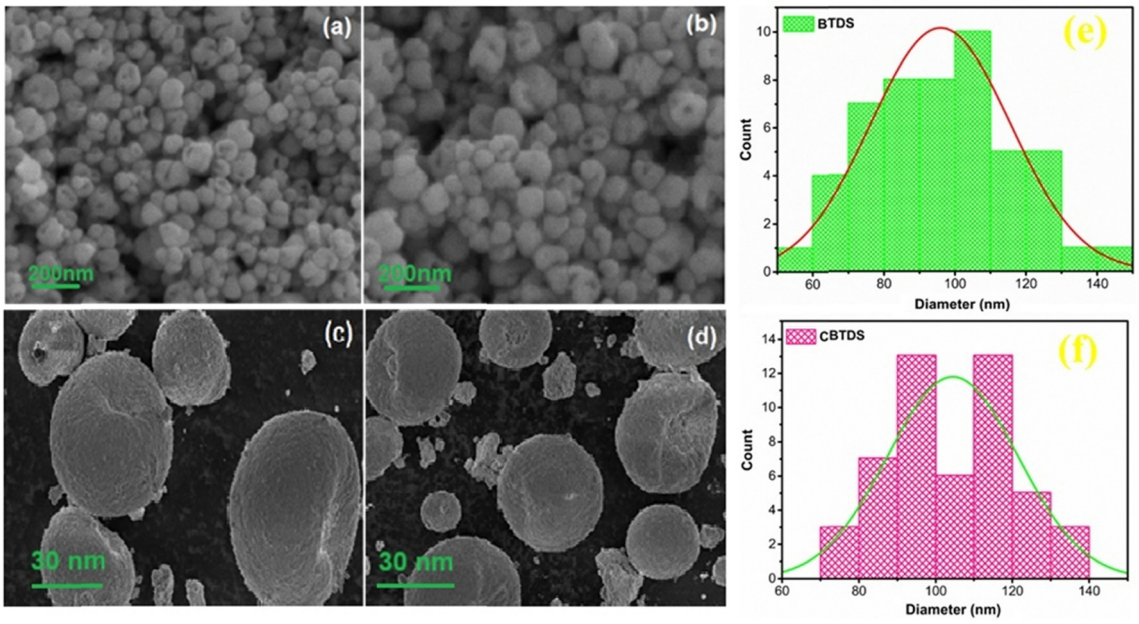

Fig. 2 FESEM images of (a) and (c) BTDS and (b) and (d) CBTDS nanostructures, (e) and (f) particle-size distribution histogram analysis of BTDS and CBTDS nanostructures.

The additional hydrothermal step resulted in minor changes in the sizes of CBTDS nanostructures, as verified by the FESEM images shown in Fig. 2(b) and (d). Moreover, the crystallite size comparison data obtained from the XRD and TEM crystallite size analysis are shown in Table S2. The results indicate an increase in the crystallite size of CBTDS because of the addition of Co^{2+} into the BTDS lattice.

Further, as shown in Fig. 2(a) and (c), BTDS nanostructures exhibit a narrow size distribution within 59 to 141 nm diameters and an average diameter of 96 nm. Similarly, as shown in Fig. 2(b) and (f), CBTDS nanostructures display a narrow size distribution within 70 to 141 nm diameters and an average diameter of 105 nm. These results show that incorporating 0.05 mol% Co into the BTDS structure increases the average diameter of the doughnut shape compared to the bare BTDS structure, which could be due to the lattice distortion. Also, the elemental mapping images indicate that the Ba (green), Ti (red), and O (cyan) elements are uniformly distributed within the BTDS structure, as displayed in Fig. S4 [SI]. Besides, based on elemental mapping and EDS analysis to confirm the composition of CBTDS nanostructures, Ba (lilac), Co (cyan), Ti (red), and O (green) elements are dispersed uniformly within the CBTDS nanostructures, as shown in Fig. S5 [SI].

The as-synthesized BTDS and CBTDS nanostructures were further analyzed by high-resolution transmission electron microscopy (HRTEM) to confirm the morphological features and crystalline phases, and their HRTEM images are shown in Fig. 3(a–d). In the HRTEM analysis, BTDS and CBTDS nanostructures demonstrated similar morphologies with notable size variations as revealed by SEM. The selected area electron diffraction (SAED) patterns confirmed the highly crystalline nature of the BTDS nanostructure (Fig. 3(e)). Further, the electron-diffraction images of the BTDS nanostructure exhibited well-resolved fringes and ring patterns for the polycrystalline torus, as shown in Fig. 3(g), and their interplanar spacings calculated were 0.4203 nm, 0.2964 nm, 0.2376 nm, and 0.2061 nm, corresponding to the (100), (110), (111), and (200) crystal planes of the tetragonal phase, respectively. Besides, as shown in Fig. 3(f) and (h), from the SAED pattern and HRTEM analysis, interplanar spacings of CBTDS nanostructures were found to be 0.4209 nm, 0.2967 nm, 0.2426 nm, and 0.2125 nm, respectively, corresponding to the (100), (110), (111), and (200) tetragonal crystal planes. Also, the HRTEM-EDS spectra of BTDS and CBTDS confirmed their respective elemental distributions [Fig. S6, SI].

Furthermore, the BET analysis of BTDS and CBTDS exhibited a typical Type-IV with Type-H3 hysteresis loop, indicating the formation of large mesopores or macrostructures. BTDS with large, agglomerated particles and a mesoporous structure showed prominent hysteresis loops compared to CBTDS. The BET estimated specific surface area of BTDS was 25.843 $m^2\ g^{-1}$, which was marginally higher than that of CBTDS (20.978 $m^2\ g^{-1}$). Similarly, the pore volumes of BTDS and CBTDS estimated by the Barrett–Joyner–Halenda (BJH) method were 0.069 $cm^3\ g^1$ and 0.047 $cm^3\ g^1$, respectively, as shown in Fig. 4 and Table S7 [SI]. The BJH pore-size distribution analysis of the nanostructures showed a unimodal mesopore distribution in both BTDS and CBTDS nanostructures. Also, BTDS and CBTDS displayed wide BJH pore-size distributions in the 3–26 nm and 3–27 nm ranges, respectively. After incorporating the Co^{2+} dopant into BTDS, a slightly increased pore size was observed, as shown in Fig. 4(b) and Table S7. Due to the incorporation of Co^{2+} into the BTDS lattice, CBTDS showed a decrease in surface area and pore volume, but a more extensive pore size distribution and pore diameter.

As evidenced by XRD and TEM analyses, the more extensive pore size distribution and pore diameter could be assigned to more porous interior structures and the presence of mesoporous structures with larger crystallites of CBTDS. The increasing pore

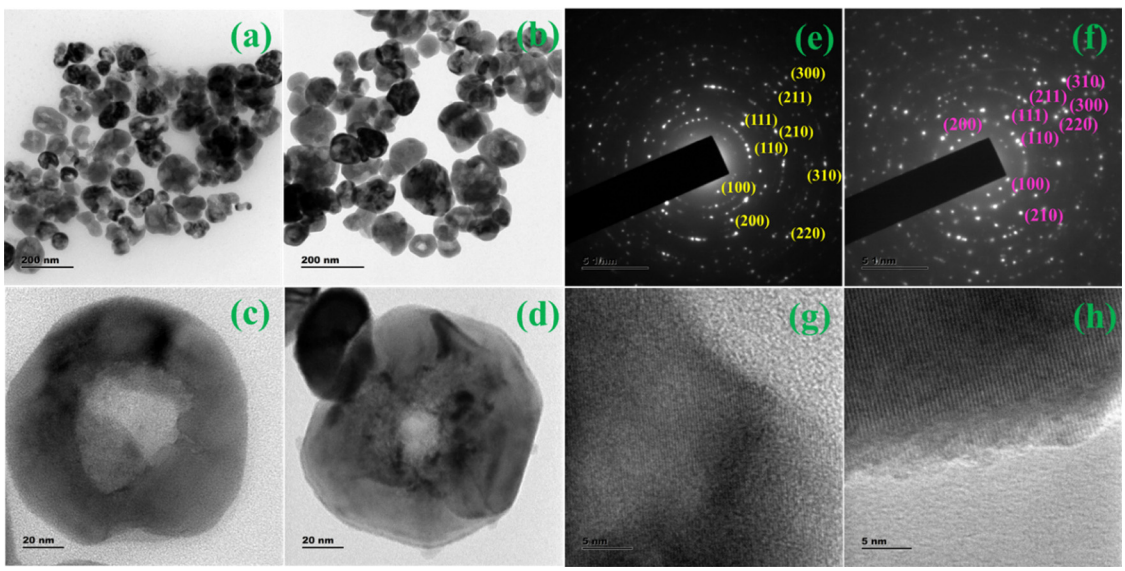

Fig. 3 Low and high magnification HRTEM images of (a) and (c) BTDS and (b) and (d) CBTDS nanostructures. (e) and (f) Selected-area electron diffraction (SAED) patterns and (g) and (h) (110) plane lattice fringes of BTDS and CBTDS nanostructures, respectively.

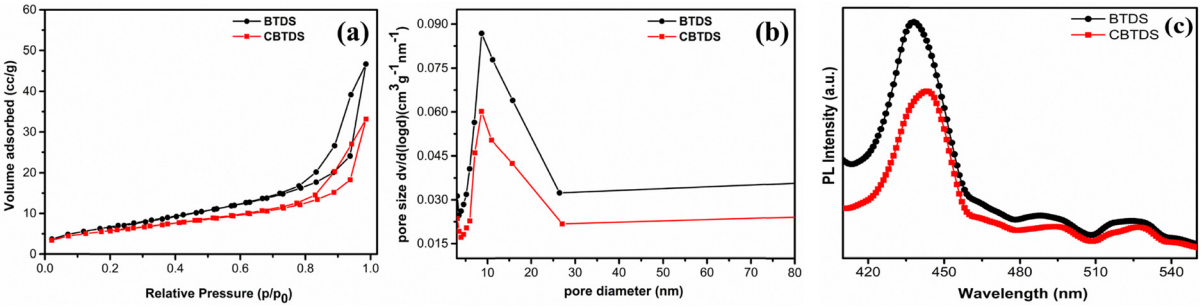

Fig. 4 (a) Traces of the N_2 adsorption–desorption isotherm of BTDS and CBDTS nanostructures, (b) pore size distribution analysis using the Barrett–Joyner–Halenda (BJH) method, and (c) steady-state photoluminescence (PL) spectra of BTDS and CBTDS nanostructures.

size distribution and pore diameter of CBTDS nanostructures could play a significant role in superior dye loading, enhanced light-scattering ability, and improved photocurrent generation in DSSCs. Typically, nanostructures with narrow pore size distributions were deemed beneficial for efficient dye loading and improved electrolyte penetration. This may result in the superior charge transfer processes at the photoanode–electrolyte interface.[26]

Light-scattering and band shift effects

To evaluate the influence of the light scattering effect and absorption properties of BTDS and CBTDS nanostructures, the UV-visible-NIR diffuse reflectance (DRS) and absorption spectra of their thin films were examined in the 200–1400 nm wavelength region, as shown in Fig. S8 [SI]. The film with a high diffuse reflectance percentage indicated a clear enhancement of the light-scattering effect, and can be utilized as a light-scattering top layer of a bilayer DSSC photoanode.[26] Among the thin films, BTDS demonstrated the maximum diffuse reflection (91%) in the visible to NIR (420–1400 nm) wavelength region. In contrast, the CBTDS thin film showed the maximum diffuse reflection (85%) in the NIR (900–1000 nm) wavelength region. The CBTDS film absorbed more visible light and exhibited a lower diffuse reflectance as compared to the BTDS film. Moreover, the optical absorbance spectra of BTDS and CBTDS thin films were recorded to understand the influence of cobalt doping in BTDS and to correlate band gap changes to the photocurrent produced in the CBTDS-based DSSCs. The optical absorption of both nanostructures was recorded in the UV-visible to near-infrared (NIR) region at wavelengths ranging from 200 to 1400 nm, as shown in Fig. S8. The broad absorption of the CBTDS thin film could be due to Co-metal doping in BTDS, shifting the absorption edge from visible light to the NIR region, and the structural distortion of the BTDS lattice contributed to the Urbach tail along with band gap narrowing.[38] As shown in Fig. S8, the thin film of CBTDS exhibited two broad absorption peaks at 520–725 nm and 980–1400 nm in the visible light to the NIR region. The peak that appeared at wavelength 520–725 nm for CBTDS could be due to Co doping raising the energy levels in BTDS just above the valence band and narrowing the band gap, resulting in the characteristic absorption in the visible and NIR regions, besides the Urbach tailing effects. This could significantly contribute to the increase in the light-harvesting ability of CBTDS over BTDS. Fig. S8(b) shows the Tauc plots obtained for the indirect band gap of BTDS and CBTDS thin films using the equation (eqn (1))[15,16,25,37]

$$\alpha h\nu = \beta(h\nu - E_g)^n \quad (1)$$

where β, h, ν, α, and E_g are optical constants, Planck's constant, photon frequency, absorption coefficient, and optical band gap energy, respectively. As shown in Fig. S8(b), the thin film band gap energies estimated from respective Tauc plots of BTDS and CBDTS indicated that the BTDS band gap was reduced from 3.1 to 2.51 eV by doping 0.05 mol% of cobalt into its lattice. The doping of Co^{2+} into Ba^{2+} caused disorder at the local sites of the host lattice ($BaTiO_3$) and manifested the Urbach states, resulting in a band gap energy of 2.51 eV for CBTDS at 0.05 mol% of Co dopant concentration.[38] The CBTDS nanostructures demonstrated a lower band gap energy, favorable for faster charge separation and slower recombination due to the ferroelectric dipoles, which is desirable for better photocurrent generation of DSSCs.

The steady-state photoluminescence (PL) spectra of BTDS and CBTDS nanostructures with an excitation wavelength of 380 nm were recorded to investigate the nanostructures' emission characteristics and localized state formation, as depicted in Fig. 4(c). Both samples displayed intense emission peaks centered at 435 nm, with a marginal shift in the peak maximum for the CBTDS sample because the cobalt dopant in the barium titanate lattice exhibits a weak, broad emission with maxima of 490 and 520 nm. The oxygen vacancies in CBTDS nanostructures can be identified by using PL maxima while comparing them to the PL maxima of BTDS nanostructures. Oxygen vacancies typically cause a red shift in the emission wavelength. This shift occurs because photo-generated electrons get trapped within the defect sites created by the oxygen vacancies. Also, the intensity of the peak at 435 nm was reduced by almost 30% in CBTDS compared to BTDS because of doping; perhaps the emission intensity of the 490 nm and 520 nm peak maxima remained closer in both samples. The localized states were formed in the BTDS and CBTDS nanostructures due to structural disorders such as reduced crystallinity, lattice defects, impurities, and polarization effects, which can also contribute to the increased emission intensity.[39] The peak that appeared

around 520 nm was ascribed to the localized states in the band gap that facilitated the electronic transition from the valence band to the conduction band. As shown in Fig. 4(c), the PL intensity of CBTDS is lower than that of BTDS, which may be due to the faster recombination kinetics between the photogenerated electrons and holes. Besides, both BTDS and CBTDS nanostructures can demonstrate the Gorbatsevich and Kopaev-type toroidal polarization effects due to their nanotorus geometry with different radii, in which toroidal dipoles formed act as solenoids containing circular vortices[40] as shown in Fig. S8(c). The toroidal domains possess continuously rotating electric dipoles based on the local polarization. Ferroelectric domains generally have electric dipoles in linear order, causing spontaneous polarization in conventional barium titanate nanostructures. Because of the geometry differences compared to the conventional ferroelectric materials, the ferroelectricity in the BTDS and CBTDS nanostructures is produced by their nanotorus geometry-dependent toroidal electric dipole moment (T) that can be expressed as (eqn (2))

$$T = (2N)^{-1} \sum_{i} (r_i) \times \delta p_i \qquad (2)$$

where p_i is the polarization of the local dipole of cell 'i' positioned at r_i. The aspect ratio $a = r/R$, *i.e.*, the ratio of the nanotorus inner (r) and outer (R) radii, influences the net toroidal moment generated in the BTDS and CBTDS nanostructures. Moreover, the aspect ratio can affect the polarization pattern and can lead to the formation of different phases of ferroelectric toroidal and hypertoroidal moments. From the TEM images (Fig. 3c and d), it can be justified that the low aspect ratio of, $a \approx 0.25$ found in the CBTDS nanostructures could offer a stable toroidal moment over the BDTS ($a \approx 0.40$) nanostructures.[40]

Electronic states, Ti^{3+}, and oxygen vacancy formation

The X-ray photoelectron spectroscopy (XPS) analysis was carried out to confirm the elemental composition, oxidation states, and electronic environments of the BTDS and CBTDS nanostructures. The survey scan XPS spectra of CBTDS [Fig. S9, SI] confirmed the presence of Ti 2p, O 1s, C 1s, Ba 3d, Co 2P, and Co 3P with the XPS signals with binding energy ranges of 457–463 eV, 529 eV, 284.8 eV, 778–793 eV, 778.25–793.53 eV, and 61 eV, respectively. All XPS peaks were calibrated using C 1s (284.8 eV B.E.), and the spectra were fitted with Lorentzian curves for each component peak. The Ba 3d XPS spectra of BTDS and CBTDS are presented in Fig. 5(a, b). In Fig. 5(a), the XPS spectrum of BTDS reveals two prominent signals at 793.39 eV and 778.10 eV energies, corresponding to spin states of Ba $3d_{3/2}$ and Ba $3d_{5/2}$, respectively.[24,41–43] Also, the Ba $3d_{3/2}$ and Ba $3d_{5/2}$ spin states can be further deconvoluted into two weaker peaks at 794.77 eV and 779.54 eV, respectively. These weaker peaks can be attributed to Ba^{2+} states, signifying a relaxed Ba–O surface phase. The presence of these states generally suggests the occurrence of oxygen vacancy-related defects in the $BaTiO_3$ structure.[17,43] Similarly, in Fig. 5(b), the XPS spectrum of CBTDS exhibits two significant peaks for Ba 3d that are slightly shifted as compared to the BTDS binding energies. These peaks are centered at 793.57 eV and 778.29 eV,[24,44] corresponding to the energies of Ba $3d_{3/2}$ and Ba $3d_{5/2}$ spin states, respectively. The narrow scan Co 2p XPS spectrum (Fig. 5c) displays a core-level XPS chemical shift for the Co 2p signal in the CBTDS spectrum. It exhibits two prominent doublet peaks at 793.53 eV and 778.25 eV, which can be assigned to the energies of Co $2p_{3/2}$ and Co $2p_{1/2}$ spin states, respectively.[17,24,45] The presence of cobalt (Co) ions in CBTDS is further confirmed by the core-level XPS chemical shift observed for the Co 2p state. The splitting of the binding energy of Co $2p_{3/2}$ and Co $2p_{1/2}$ spin states can be

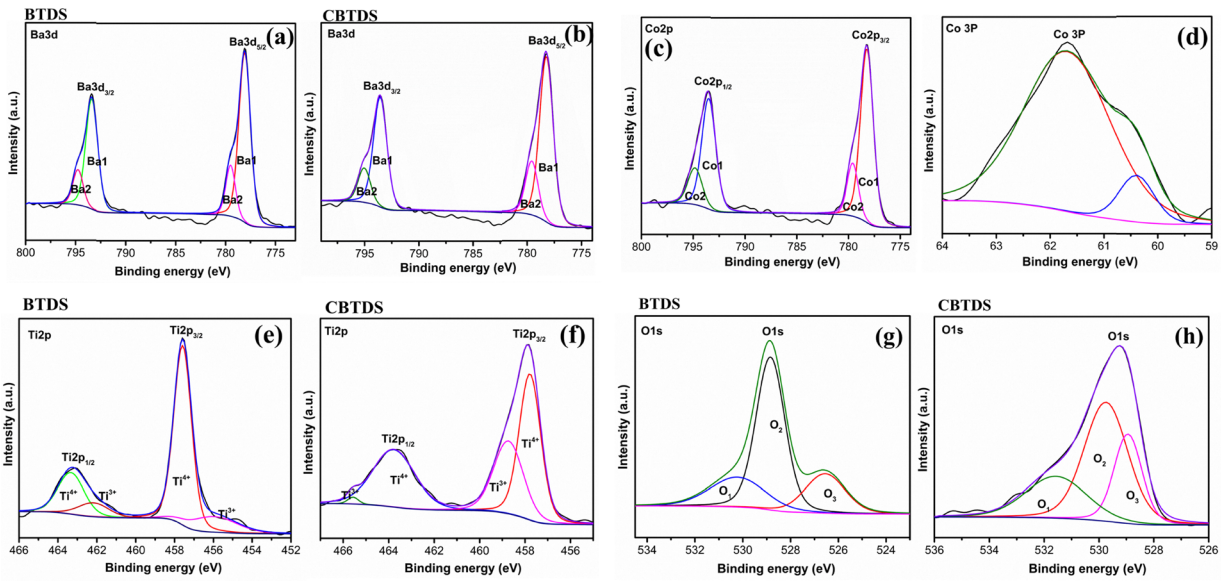

Fig. 5 (a) and (b) High-resolution XPS spectrum of Ba 3d peaks of BTDS and CBTDS, (c) XPS spectrum of Co 2p peaks, (d) XPS spectrum of Co 3p peaks, (e) and (f) XPS spectrum of Ti 2p peaks, and (g) and (h) XPS spectrum of O 1s peaks.

assigned to the incorporation of cobalt (Co) into BTDS, as the Co 2p spin states appear as peaks at 793.61 eV and 778.28 eV, analogous to the core-level XPS signals of Co^{3+} ions.[24,44,45] Additionally, the Co $2p_{3/2}$ and Co $2p_{1/2}$ spin states can be deconvoluted into weaker peaks at 794.81 eV and 779.58 eV, representing Co^{2+} states, respectively. Due to the closer proximity of the Ba 3d and Co 2p peaks, separating the characteristic signals of Co 3d was challenging. However, the presence of Co^{2+} ions in the BTDS crystal structure was ascribed to the lower binding energies of CBTDS compared to that of BTDS. Further, the Co^{2+} ions' 3p signal confirmed the CBTDS nanostructures (Fig. 5d), by demonstrating a peak centered at 61.68 eV.[24,42] Fig. 5(e) shows the binding energies located at 457.59 eV and 463.34 eV, which accounted for the Ti $2p_{3/2}$ and Ti $2p_{1/2}$ spin states, respectively, of BTDS.[17,41,42,46] This indicates a Ti^{4+} oxidation state in the perovskite $BaTiO_3$ structure, thus confirming the presence of Ti–O and Ba–O bonds. In addition, the Ti $2p_{3/2}$ and Ti $2p_{1/2}$ signals could be deconvoluted into two sub-signals at 455.69 eV and 462.16 eV, respectively, indicating the presence of Ti^{3+} states, which characteristically signify the formation of oxygen vacancy-related defects in BTDS. Similarly, due to the Co-doping effects on the Ti 2p XPS peaks, CBTDS showed slightly shifted binding energy values. Fig. 5(f) shows the splitting of Ti $2p_{3/2}$ and Ti $2p_{1/2}$ spin states with binding oxidation state in the perovskite $CoBaTiO_3$ structure. The Ti $2p_{3/2}$ and Ti $2p_{1/2}$ peaks could be further deconvoluted into two subpeaks located at 458.76 eV and 465.57 eV, respectively, indicating the presence of Ti^{3+} states and oxygen vacancy-related defects in CBTDS. Due to Co-doping in the $BaTiO_3$ lattice, the CBTDS structure exhibits a rise in the Ti^{3+} peak intensity and a reduction in the Ti^{4+} peak intensity compared to the BTDS structure. Besides, the decreasing area of the Ti^{4+} peak suggests a decrease in $CoBaTiO_3$ and the potential formation of Ti–O–Ba or Co–O–Ba bonds. This is likely due to the Co metal doping, which may involve the replacement of either Ba or Ti species within the $BaTiO_3$ lattice through substitution.[24]

Moreover, the O 1s spectrum of the BTDS structure depicted in Fig. 5(g) exhibited a major signal, which is resolved into three distinct signals at 526.53 eV, 529.03 eV, and 530.26 eV, corresponding to specific chemical environments: (O–Ti–O, O–Ba–O), (C–O, Ba–O), and C–O–H groups, respectively.[41,42,44,46] The signal at 529.03 eV is assigned to the oxygen functionalities, such as lattice oxygen (O–Ti–O, O–Ba–O bonding) and hydroxyl groups on the titanate surfaces. Meanwhile, the signal at 530.26 eV is assigned to the oxygen species associated with C–O–H and hydroxyl groups. Finally, the peak at 526.53 eV indicates the manifestation of interactions with the Ba–O vacancy sites on the surfaces.[24] Consequently, the observed peaks collectively indicate the occurrence of oxygen vacancy-related defects within the BTDS structure. Similarly, the O 1s spectrum of the CBTDS sample depicted in Fig. 5(h) demonstrated a major signal, which is deconvoluted into three dissimilar signals at 528.93 eV, 529.74 eV, and 531.60 eV, corresponding to specific chemical environments: (O–Ti–O, O–Ba–O, O–Co–O), (C–O, Ba–O, Co–O), and C–O–H bonds, respectively. The peak at 529.93 eV is attributed to adsorbed oxygen species interacting with lattice oxygen (O–Ti–O, O–Ba–O, O–Co–O bonding) and –O–H groups on the titanate surfaces. Meanwhile, the peak at 531.60 eV is assigned to adsorbed oxygen species associated with C–O–H bonds and hydroxyl groups. The peak at 528.93 eV indicates the presence of adsorbed oxygen species at the Ba–O and Co–O surface vacancy sites.[24] The presence of O vacancies with signals in the same spectral region in CBTDS indicates the promising magnetic and electrical behaviors due to the favorable chemical environment when Co replaces Ti.[24,45] When Co replaced Ti in the lattice, it supported the preservation of ferromagnetic behavior and enhanced the dipole electric field with higher electrical conductivity in CBTDS than BDTS.

Photovoltaic characterization

To evaluate the morphology-dependent light harvesting ability of the toroidal ferroelectric BTDS and CBTDS nanostructures and their photovoltaic performance, their respective bilayer photoelectrodes, TNP + BTDS and TNP + CBTDS, were constructed as DSSCs. Fig. 6(a) shows the *J–V* comparison curves of DSSCs constructed with TNP + BTDS and TNP + CBTDS photoelectrodes, and Table 3 shows their photovoltaic performance data. The Co metal doping influenced the light absorption properties of CBTDS nanostructures in many ways, such as superior visible and near-infrared light absorbing properties,

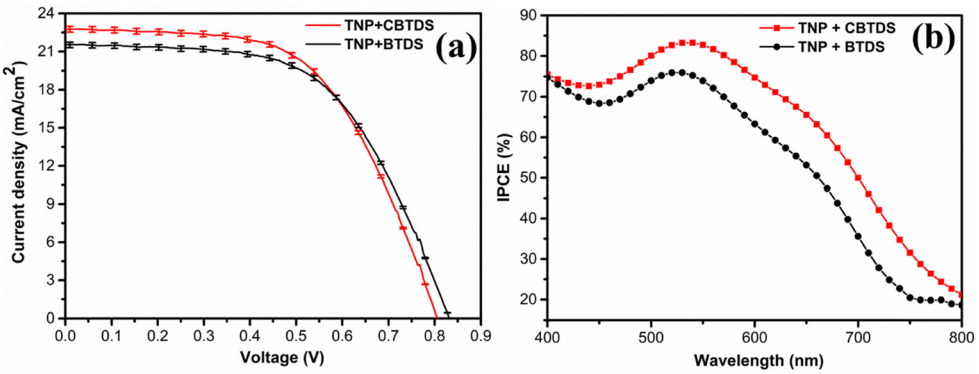

Fig. 6 (a) Photovoltaic *J–V* curves of DSSCs constructed using TNP + BTDS and TNP + CBTDS bilayer photoelectrodes. (b) IPCE spectra of DSSCs made using TNP + BTDS and TNP + CBTDS bilayer photoelectrodes.

toroidal ferroelectric dipole moment-induced effects on photo-induced charge separation, and improved dye-loading capacity. However, the BTDS nanostructure demonstrated a higher diffuse reflectance of 91% in the 350–1400 nm wavelength region, supporting its superior light scattering ability than the CBTDS nanostructures (85%) in the 350–1400 nm wavelength region. Interestingly, the UV-vis absorption spectrum of the CBTDS film indicated notable light absorption in the 520–725 nm and 980–1400 nm wavelength regions, which can contribute to the increase of the light-harvesting ability of the TNP + CBTDS bilayer photoelectrode for improving the photocurrent generation in its DSSCs, as shown in Fig. 6(a). In addition, Co-metal doping reduces the bandgap (from 3.1 eV to 2.51 eV) of the barium titanate film of the DSSC photoelectrode, resulting in enhanced light absorption in the near-infrared region and amplified exciton formation, thereby boosting the DSSC's photocurrent (J_{SC}). Co-metal doping in the BTDS-based light-scattering layer in the photoanode minimizes energy losses by the slower charge recombination due to its toroidal ferroelectric dipole-induced effects, as confirmed by the PL analysis.

Furthermore, CBTDS nanostructures with high concentrations of oxygen vacancies and Ti^{3+} ions can facilitate charge separation and improve charge carrier mobility, leading to more efficient energy conversion in the DSSCs. As a result, the TNP + CBTDS bilayer photoelectrode, having the CBTDS sublayer, exhibited better light absorption, superior photosensitizing behavior, and a toroidal ferroelectric dipole, supporting exceptional charge migration. In contrast, the TNP + BTDS bilayer photoelectrode had superior specific surface area and pore volume but suffered in pore size distribution and diameter, affecting its photoelectrode film's dye loading. The optimal pore size and diameter that could help achieve maximum dye loading of the photoelectrode are reported in the literature.[37,38] In this work, the crystallite size, pore size, and pore diameter of the CBTDS nanostructure played a significant role in the superior dye uptake and greater photocurrent generation of its photoelectrode, as shown in Table 1.

In DSSCs, the TNP + BTDS bilayer photoelectrode generated a maximum photocurrent density (J_{SC}) of 21.53 ± 0.21 mA cm^{-2} and a PCE of 10.01 ± 0.40%, and the TNP + CBTDS bilayer photoelectrode produced a J_{SC} of 22.81 ± 0.15 mA cm^{-2} and a PCE of 10.29 ± 0.44%. The TNP + CBTDS bilayer photoelectrode generated an open circuit voltage (V_{OC}) of 0.81 ± 0.01 V, which was less than the V_{OC} of the TNP + BTDS bilayer electrode (0.83 ± 0.01 V) because the incorporation of Co into BTDS narrowed the band gap by introducing mid-gap states, as evident from optical band gap calculations. In addition, CBTDS had a lower band gap and a higher toroidal ferroelectric dipole-induced electric field than BTDS in the bilayer photoelectrode. These observations indicated that the visible light absorption and toroidal ferroelectric behavior of CBTDS favored increasing the number of photogenerated charge carriers, resulting in a higher photocurrent generation of the TNP + CBTDS bilayer photoelectrode-based DSSC. To support this, the photovoltaic *J–V* performance of CBTDS and TNP + CBTDS without dye loading as monolayer and bilayer photoelectrodes of DSSCs was also investigated separately (Fig. S11). The DSSCs of CBTDS and TNP + CBTDS photoelectrodes demonstrated J_{SC} of 3.06 mA cm^{-2} and 5.91 mA cm^{-2}, V_{OC} of 0.52 V and 0.64 V, and PCE of 0.65% and 1.78%, respectively. The *J–V* results demonstrated that the Co metal ion dopant in the BTDS lattice of the CBTDS nanostructures made them a better photon-absorbing layer and effectively formed the photogenerated electrons for the increased charge collection at the FTO substrate in the TNP + CBTDS photoelectrode, resulting in the increased J_{SC} value. Similarly, the V_{OC} of solar cells made of a CBTDS monolayer photoelectrode was 200 mV less than the V_{OC} of DSSCs constructed with the TNP + CBTDS photoelectrode due to the higher band gap of TiO_2 (3.2 eV) and possibly due to band mixing.

To understand the photocurrent generation and light-harvesting abilities of BTDS and CBTDS nanostructures in various light wavelength regions, the incident photon to current conversion efficiency (IPCE) of their DSSCs was recorded. The IPCE responses of solar cells can be expressed as (eqn (3))

$$\mathrm{IPCE}(\lambda) = \eta_{\mathrm{lhe}}(\lambda)\cdot\varphi_{\mathrm{in}}\cdot\eta_{\mathrm{col}} \quad (3)$$

where η_{lhe} is the light-harvesting efficiency, φ_{in} the charge injection efficiency, and η_{col} the charge collection efficiency.[47] The dye uptake value and the IPCE data can determine the LHE. The IPCEs of TNP + BTDS and TNP + CBTDS bilayer photoanode-based DSSCs are shown in Fig. 6(b). The IPCE of all DSSCs indicated peaks analogous to the first excitonic absorption of the N719 dye in the 520–530 nm range. IPCE values for DSSCs of TNP + BTDS and TNP + CBTDS bilayer photoelectrodes showed peak maxima of 76.10% and 83.30%, respectively. The highest IPCE spectral value of 83.30% obtained for the TNP + CBTDS bilayer photoanode-based DSSC indicated the optimum light scattering ability, extended visible and NIR light absorption, enhanced dye uptake capacity, and favorable ferroelectric behavior of the photoanode, collectively improving the photocurrent density of its DSSC. In contrast, its counterpart, the TNP + BTDS bilayer photoanode in DSSCs, showed superior light scattering ability but poor dye loading and insignificant visible and NIR light absorption, which reduces the photocurrent density. As a result, its TNP + CBTDS bilayer photoelectrode generated the highest IPCE of 83%, due to the electrons that are photo-generated by the visible and NIR active material

Table 1 Photovoltaic and dye uptake parameters of DSSC bilayer photoanodes

Photoanode	J_{SC} (mA cm^{-2})	V_{OC} (V)	FF	PCE (%)	IPCE (%)	Amount of dye loaded (μmol cm^{-2})
TNP + CBTDS	22.81 ± 0.15	0.81 ± 0.01	0.56 ± 0.04	10.29 ± 0.44	83.30	7.87
TNP + BTDS	21.53 ± 0.21	0.83 ± 0.01	0.55 ± 0.09	10.01 ± 0.40	76.10	6.27

being more accessible to inject into the conducting electrode with optimum light absorption, charge transport, and toroidal ferroelectric dipole-induced electric field effects that can increase the photocurrent of the DSSC significantly.

Charge transfer processes at the photoanode/electrolyte interface

As shown in Fig. 7(a) and Table 2, the charge recombination resistance of DSSCs decreased from 248.34 Ohm cm^2 to 186.61 Ohm cm^2 when the bilayer photoanode was changed from TNP + CBTDS to TNP + BTDS, indicating a higher charge recombination resistance (R_{ct}) of the TNP + CBTDS photoanode. The Nyquist plots recorded for the DSSCs in the applied voltage range of −0.4 V to −0.8 V revealed that at −0.7 V, each photoelectrode charge transport resistance R_t produced a straight line within the big semicircle produced by R_{ct}, as shown in Fig. 8. R_t is a good sign of charge transport *via* the mesoporous oxide bilayers in the photoelectrodes. Fig. 7(b) exhibits the EIS frequency *vs.* phase angle (Bode) plots of bilayer photoanode based DSSCs that are used to estimate the electron lifetime (τ_n) using the equation $\tau_n = 1/(2\pi f_{max})$, where f_{max} refers to the low-frequency peak in the plot. As shown in Table 2, the TNP + BTDS bilayer photoanode produced significantly longer electron lifetime (50.07 ms) than the TNP + BTDS bilayer photoanode (24.02 ms) in DSSCs. Typically, the large charge recombination resistance favors a longer electron lifetime (τ_n) in the DSSCs. Fig. 7(b) confirms the long electron lifetime due to the 3D mesoporous toroid structure, extending the electron mean free path. As a result, the TNP + CBTDS photoanode exhibited a longer electron lifetime than the TNP + BTDS photoanode. Thus, the extended electron mean free path and the reduced electron transport resistance value of the TNP + CBTDS bilayer photoanode produced an increased electron lifetime, longer diffusion length, and enhanced charge collection yield in the DSSC, as shown in Table 2.

Besides, the bilayer photoelectrode loaded with CBTDS nanostructures, showing comparatively smaller BET surface area and porosity percentage values, generated better chemical capacitance at higher applied potentials closer to V_{OC}, as shown in Fig. S12 [SI]. In contrast, the BTDS nanostructure bilayer photoelectrode produced lower chemical capacitance at higher bias potential despite showing good surface area and porosity values.[48–50] This could be due to the reduced double-layer capacitance contribution to the total chemical capacitance estimated at higher applied potentials.[51] Among BTDS and CBTDS nanostructures, CBTDS showed a good chemical capacitance value due to the favorable pore size and porosity, allowing better redox electrolyte penetration in the TiO_2/CBTDS network for the rapid regeneration of oxidized dyes. Also, the charge recombination lifetime (τ_n) at the photoelectrode/electrolyte interface can be estimated using eqn (4):[51,52]

$$\tau_n = R_{ct} \cdot C_\mu \quad (4)$$

where R_{ct} denotes the charge transfer resistance and C_μ denotes the chemical capacitance. The charge transport properties of DSSC photoelectrodes have been widely reported from the effective diffusion coefficient D_n, obtained from parameters like C_μ, R_{ct}, and R_t by eqn (5):[52]

$$D_n = \frac{L^2}{R_t \cdot C_\mu}; \quad L_n = \sqrt{(\tau_n D_n)}; \quad \eta_{cc} = \frac{1}{\left[1 + \left(\frac{R_t}{R_{ct}}\right)\right]} \quad (5)$$

L indicates the film thickness of a photoelectrode. Usually, D_n and τ_n have an exponential relationship with the applied potential, as shown in Fig. S14. The TNP + CBTDS photoanode showed the highest D_n at the applied voltage range of −0.4 V

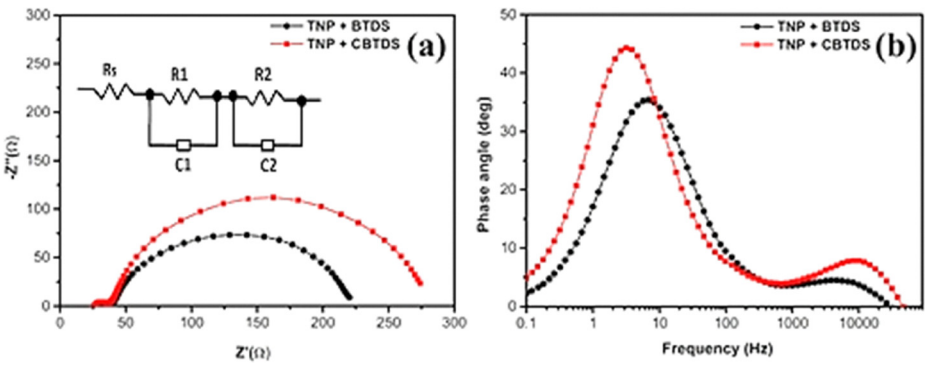

Fig. 7 Electrochemical impedance spectroscopy (EIS) of DSSCs of TNP + BTDS and TNP + CBTDS photoelectrodes at an applied potential of −0.8 V: (a) Nyquist plots with an equivalent circuit as the inset and (b) Bode plots.

Table 2 EIS parameters determined from Nyquist plots recorded at an applied potential of −0.8 V

Photoanode	R_S (Ohm cm^2)	R_{ct} (Ohm cm^2)	R_{tr} (Ohm cm^2)	Chemical capacitance (F)	Electron lifetime (ms)	Electron recombination lifetime (ms)	Diffusion length (μm)	Charge collection efficiency (%)
TNP + BTDS	34.27	186.61	29.83	3.14×10^{-4}	24.02	58.59	37.58	86.22
TNP + CBTDS	25.83	248.34	23.34	5.01×10^{-4}	50.07	124.41	48.93	91.41

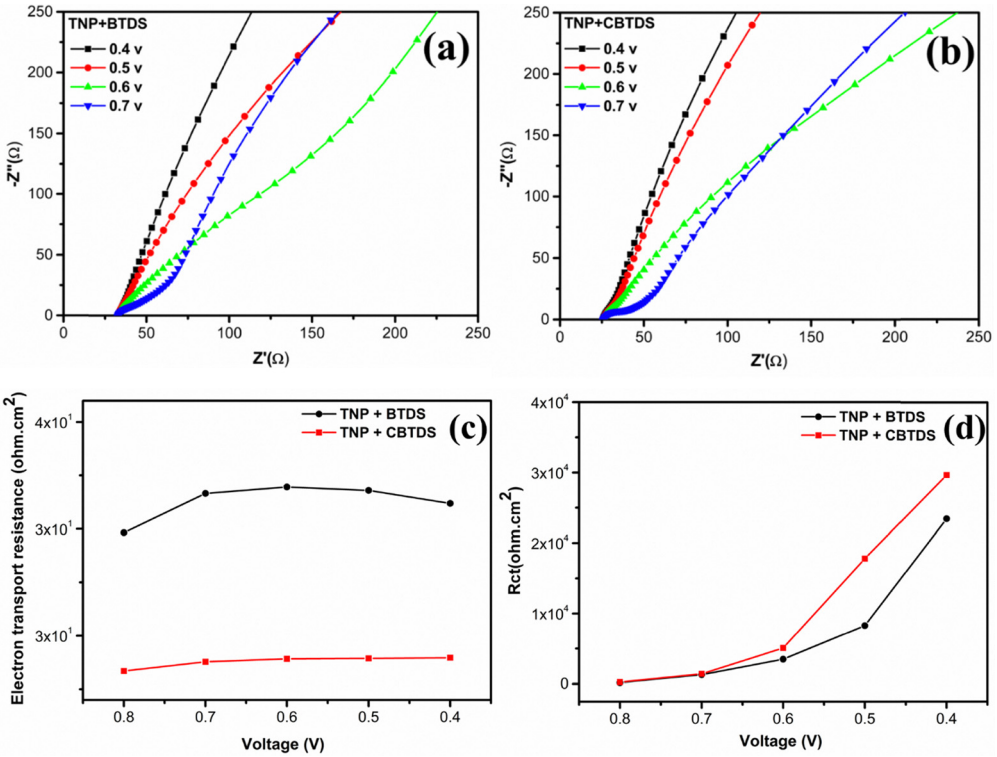

Fig. 8 (a) and (b) EIS Nyquist plots of TNP + BTDS and TNP + CBTDS bi-layer photoanode-based DSSCs recorded at an applied bias potential of −0.4 V to −0.7 V under dark conditions. (c) Electron recombination resistance and (d) electron transport resistance at an applied bias potential of −0.4 V to −0.8 V under dark conditions. The EIS parameters of TNP + BTDS and TNP + CBTDS bi-layer photoanode-based DSSCs obtained from the Nyquist plots recorded at an applied bias potential of −0.8 V and fitted with an equivalent circuit (above).

and −0.8 V compared to the TNP + BTDS bilayer photoanode. The electron diffusion length of the bilayer photoelectrode at the photoelectrode/electrolyte interface can be obtained by using the above equation for L_n. Generally, R_{ct} and R_t values of bilayer photoelectrodes can influence the electron diffusion within the BTDS- or CBTDS-containing sublayer since L_n is the average distance electrons travel through the conduction band before recombining with holes.[52,53] Moreover, Fig. S12(c) shows the electron diffusion length determined at an applied voltage of −0.4 V and −0.8 V. The curves indicate that a low R_t of a bilayer affects the electron diffusion within the doughnut sublayer. The charge collection efficiency (η_{cc}) of the bilayer photoelectrode at the electrode/electrolyte interface can be estimated using eqn (5). The TNP + CBTDS photoanode has a longer electron diffusion length and higher η_{cc} within its three-dimensional morphology. These findings support increased J_{SC} observed for the TNP + CBTDS photoanode-based DSSC. Also, compared to the literature-reported barium titanate-based photoanodes (Table 3), the TNP + CBTDS photoanode produced the highest PCE value due to its favorable sublayer morphology for the superior light-to-current conversion.

Table 3 Comparison of highly efficient barium titanate-based photoanode and photocatalyst materials available in the literature with the results of this work

DSSCs			
Photoanode material used	Single- or bi-layer DSSCs	Photovoltaic efficiency (%)	Ref.
$BaTiO_3/TiO_2$ nanotubes	Hybrid single layer	10.15	Chen *et al.*[12]
TiO_2 + $BaTiO_3$ nanocomposite	Single layer	9.40	Asgari *et al.*[8]
TiO_2 NPs + $BaTiO_3$ nanowires/GNP	Double layer	9.92	Murali *et al.*[26]
TiO_2 NPs + BTDS	Double layer	10.01	This work
TiO_2 NPs + CBTDS	Double layer	10.29	This work
Dye degradation			
Photocatalyst material used	Light source	Dye removal efficiency (%)	Ref.
Textured and poled $BaTiO_3$ NR array	No	97	Chiu *et al.*[30]
Ag–$BaTiO_3$	Xenon	83	Xu *et al.*[56]
$BaTiO_3$–MnO_2	UVA	70	Biernecka *et al.*[57]
BTDS	Xenon	76	This work
CBTDS	Xenon	86	This work

Photocatalytic dye degradation study

The BTDS and CBDTS nanostructures were employed as rhodamine B dye degradation photocatalysts under AM1.5 G conditions using standard solar light irradiation (100 mW cm^{-2}). Fig. 9(a) and (b) show the absorption spectra of Rhodamine B dye recorded over 75 min at the time interval of every 15 min upon photocatalytic reaction with BTDS and CBDTS

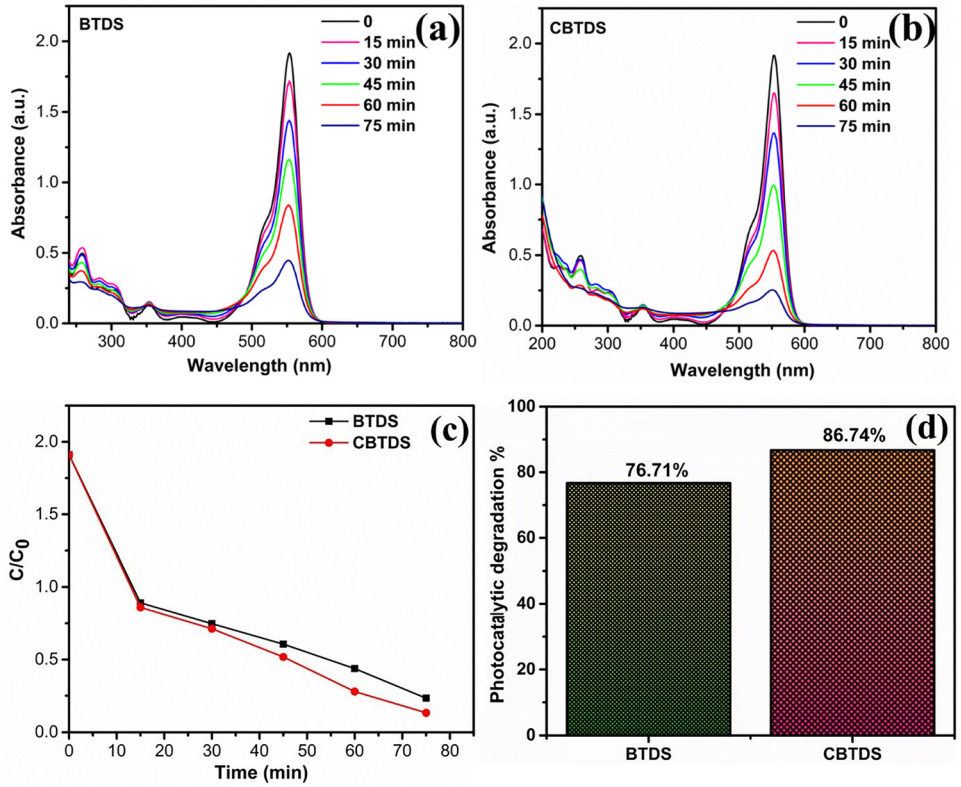

Fig. 9 Absorption spectra recorded during the photocatalytic degradation of rhodamine B using (a) BTDS and (b) CBTDS nanostructures as a catalyst. (c) C/C_0 *vs.* time for photodegradation of rhodamine B dye solution. (d) Photocatalytic degradation percentage for the BTDS and CBTDS samples.

nanostructures. The concentration of rhodamine B was ascertained from the maximum absorbance value at λ = 544 nm obtained from the UV-vis absorption spectra, as shown in Fig. 8(a) and (b). Dye degradation (%) was calculated using eqn (6):[29,30,50,51]

$$\text{Degradation } (\%) = \frac{C_0 - C}{C_0} \times 100 \qquad (6)$$

where C_0 is the initial concentration and C is the concentration at different time intervals obtained from the solution.[54,55] The concentration after adsorption equilibrium (C_0) was used to determine the initial concentration of rhodamine B. Besides, the C/C_0 ratio was calculated to compare the dye degradation rates by the BTDS and CBTDS photocatalysts over 75 min, as shown in Fig. 9(c). Fig. 9(d) show the overall photocatalytic degradation percentage after 75 min using the BTDS and CBTDS catalysts. The CBTDS nanostructure demonstrated a reasonably good photocatalytic degradation activity of 86.74% for rhodamine B dye over 75 min, indicating superior activity than pure BTDS nanostructures, which yielded a better value of 76.71% (Fig. 9) as compared to the similar types of photocatalytic systems dye degradation percentages reported in the literature (Table 3). We assumed that the CBTDS nanostructures having a lower band gap energy induced the superior visible light absorption behavior of their 3D nanostructures for better degradation of the organic dye. Previous studies have indicated that electrostatic interactions between the nanostructures and the dye caused enhanced photocatalytic activity, which was one of the crucial factors in determining dye photodegradation efficiency by the BTDS and CBTDS-based photocatalytic systems.[56,57] Lower photocatalytic activity observed for the BTDS nanostructures was due to their poor visible light absorption, signifying a new photocatalytic mechanism in which Co^{2+} dopant incorporation into the BTDS lattice prompted the CBTDS nanostructures to act as a visible and near-infrared light absorbing ferroelectric photocatalyst having toroidal polarization that induces strong anisotropic charge separation. Thus, the toroidal ferroelectric dipoles induced superior charge separation and reduced band gap energy, supporting the superior sensitizing behaviors of the CBTDS nanostructures, which in turn served as an enhanced degradation photocatalyst of the organic dye.

Conclusions

In summary, 3D doughnut-shaped barium titanate and cobalt-doped barium titanate multi-functional nanostructures, BTDS and CBTDS, respectively, were prepared by a multi-step hydrothermal process from a 1D hydrogen titanate nanowire (HTNW) precursor. Subsequently, these nanostructures were investigated as a light-scattering material of the bilayer DSSC

photoanode and as a photocatalyst for rhodamine dye degradation. In the DSSC application, the TNP + CBTDS photoanode showed a rise in pore size and pore diameter, significantly improving the dye uptake of its bilayer. In addition, the TNP + CBTDS photoanode demonstrated an enhanced light scattering effect, increased light harvesting ability, and ferroelectric-induced dipole electric field effects among the bilayer DSSC photoanodes prepared. As a result, the TNP + CBTDS photoanode showed an excellent PCE of 10.29 ± 0.44% due to the paradigm function of its CBTDS sublayer, which demonstrated superior toroidal ferroelectric dipole-induced charge separation, longer diffusion length, and higher charge collection yield. Besides, the photocatalytic dye degradation studies using the BTDS and CBTDS photocatalysts for the rhodamine B dye revealed a degradation efficiency of 76.71% and 86.74%, respectively. These results suggest that the toroidal ferroelectric CBTDS nanostructures behaved as a highly adaptable energy conversion material capable of demonstrating superior light scattering and absorbing ability, better charge separation, and higher charge collection yield, supporting the fabrication of highly efficient DSSCs and effective photocatalytic dye degradation systems.

Author contributions

Murali Balu: conceptualization; data curation; formal analysis; investigation; methodology; visualization; and writing – original draft. Duraisamy Kumaresan: conceptualization; formal analysis; funding acquisition; investigation; methodology; project administration; resources; supervision; validation; and writing - review & editing. R. Krishna Prasad: data curation; visualization; and writing – original draft. Subhash Kalidindi: data curation; formal analysis; investigation; and writing – original draft.

Conflicts of interest

There are no conflicts to declare.

Data availability

The experimental data will be made available upon request.

Supplementary information (SI) is available. Supplementary information: additional experimental and spectral data, and crystallographic data. See DOI: **https://doi.org/10.1039/d5qm00765h**.

Acknowledgements

The authors thank Amrita Vishwa Vidyapeetham for providing the facility and funding needed to perform this research work. MB and DK express gratitude to DST CERI for the financial support of the characterization instruments utilized in this work.

Notes and references

1 S. P. Kharat, S. K. Gaikwad, P. G. Nalam, R. C. Kambale, A. R. James, Y. D. Kolekar and C. V. Ramana, Effect of Crystal Structure and Phase on the Dielectric, Ferroelectric, and Piezoelectric Properties of Ca^{2+}- and Zr^{4+}-Substituted Barium Titanate, *Cryst. Growth Des.*, 2022, **22**, 5571.

2 Y. Niu, F. Zhang, Z. Zhang, X. Zhang and Z. J. Wang, High energy storage properties achieved in 0.94(Bi0.5Na0.5)TiO3-0.06BaTiO3 based relaxor ferroelectric ceramics via high-entropy design, *Ceram. Int.*, 2024, **50**, 22662–22670.

3 G. G. Bhanu and B. M. Rao, Free-standing arrays of $BaTiO_3$ nanotubes for non-enzymatic glucose sensing & hydrophobic coating applications, *Nano Express*, 2024, **5**, 025010.

4 M. Li, Z. Li, S. Yaseen, N. Cui, P. Li, J. Sun, J. Liu, X. Lü and L. Gu, High-performance piezoelectric nanogenerator based on aligned single-crystal $BaTiO_3$ nanowires for self-powered applications, *Chem. Eng. J.*, 2025, **516**, 163834.

5 C. Deng, Y. Zhang, D. Yang, H. Zhang and M. Zhu, Recent Progress on Barium Titanate-Based Ferroelectrics for Sensor Applications, *Adv. Sens. Res.*, 2024, **3**, 2300168.

6 M. Ma, M. Ruan, B. Li, Y. Zhang, Y. Sun, K. Ruan and X. Liu, Coupling pyroelectric fields and donor doping to adjust Curie temperature and band structure to access to highly efficient $BaTiO_3$ photoelectrodes for dye degradation, *Appl. Surf. Sci.*, 2025, **682**, 161779.

7 A. Karvounis, F. Timpu, V. V. Vogler-Neuling, R. Savo and R. Grange, Barium Titanate Nanostructures and Thin Films for Photonics, *Adv. Opt. Mater.*, 2020, **8**(24), 2001249.

8 H. Asgari, M. Mohammad and R. Mohammadi, *J. Am. Ceram. Soc.*, 2017, 1.

9 H. Itasaka, Z. Liu, K. Mimura and K. Hamamoto, Ultra-thin barium titanate nanocrystal monolayer capacitor with graphene electrode, *Appl. Phys. Lett.*, 2023, **123**, 092903.

10 P. Xue, H. Wu, W. Xia, Z. Pei, Y. Lu and X. Zhu, Molten salt synthesis of $BaTiO_3$ nanorods: Dielectric, optical properties, and structural characterizations, *J. Am. Ceram. Soc.*, 2019, **102**(5), 2325.

11 Y. Wang, X. Li, L. Sun, H. Yuan and X. Sun, Efficient piezo-photocatalytic production of hydrogen by Ti_3C_2 MXene quantum dots modified $BaTiO_3$ nanowires, *J. Photochem. Photobiol., A*, 2026, **470**, 116649.

12 H. Chen, Y. H. Wu, H. Ma, J. B. Shi, X. W. Pan, B. X. Lei and Z. F. Sun, Dye-sensitized titanium dioxide nanotube array solar cells with superior performance induced by ferroelectric barium titanate, *Thin Solid Films*, 2020, **709**, 138205.

13 I. Olaniyan, J. Albert, B. Canabarro, H. Lu, S. Wiesner, N. Cherkashin, A. Gruverman, S. S. Chardon, D. J. Kim and C. Dubourdieu, Ferroelectricity in Single-Crystalline $BaTiO_3$ Nanodisks on Silicon, *Adv. Funct. Mater.*, 2025, **35**, e07905.

14 K. G. Baiju, B. Murali and D. Kumaresan, Synthesis of hierarchical barium titanate micro flowers with superior light-harvesting characteristics for dye sensitized solar cells, *Mater. Res. Express*, 2018, **149**, 107817.

15 K. G. Baiju, B. Murali and D. Kumaresan, Ferroelectric barium titanate microspheres with superior light-scattering

ability for the performance enhancements of flexible polymer dye sensitized solar cells and photodetectors, *Sol. Energy*, 2021, **224**, 93–101.

16 Y. Liu, X. Wang, Y. Qiao, M. Min, L. Wang, H. Shan and T. Deng, Pyroelectric Synthesis of Metal–BaTiO3 Hybrid Nanoparticles with Enhanced Pyrocatalytic Performance, *ACS Sustainable Chem. Eng.*, 2018, **7**(2), 2602.

17 D. Pradhan, H. S. Mohanty, S. Kumari, K. Bhoi, N. Tang, M. M. Rahaman, D. K. Pradhan, A. Kumar and P. D. Rack, Ferroic phase transitions and magnetoelectric coupling in cobalt-doped $BaTiO_3$, *J. Mater. Chem. C*, 2021, **9**(37), 12694.

18 A. Rani, J. Kolte and P. Gopalan, Structural, electrical, magnetic and magnetoelectric properties of Co-doped $BaTiO_3$ multiferroic ceramics, *Ceram. Int.*, 2018, **44**(14), 16703–16711.

19 T. L. Phan, P. D. Thang, T. A. Ho, T. V. Manh, T. D. Thanh, V. D. Lam, N. T. Dang and S. C. Yu, Local geometric and electronic structures and origin of magnetism in Co-doped BaTiO3 multiferroics, *J. Appl. Phys.*, 2015, **117**, 17D904.

20 T. Costanzo, J. McCracken, G. Caruntu and A. Rotaru, Quasi-Monodisperse Transition-Metal-Doped $BaTiO_3$ (M = Cr, Mn, Fe, Co) Colloidal Nanocrystals with Multiferroic Properties, *ACS Appl. Nano Mater.*, 2018, **1**(9), 4863.

21 Z. Hu, V. Koval, Y. Yue, M. Zhang, C. Jia, I. Abrahams and H. Yan, Structural evolution and coexistence of ferroelectricity and antiferromagnetism in Fe, Nb co-doped $BaTiO_3$ ceramics, *J. Eur. Ceram. Soc.*, 2023, **43**, 2460–2468.

22 E. V. Ramana, S. M. Yang, R. Jung, M. H. Jung, B. W. Lee and C. U. Jung, Ferroelectric and magnetic properties of Fe-doped $BaTiO_3$ thin films grown by the pulsed laser deposition, *J. Appl. Phys.*, 2013, **113**, 187219.

23 L. B. Luo, Y. G. Zhao, H. F. Tian, J. J. Yang, H. Y. Zhang, J. Q. Li, J. J. Ding, B. He, S. Q. Wei and C. Gao, Room-temperature ferromagnetism in the Co-doped thin films, *Appl. Phys. Lett.*, 2008, **92**, 232507.

24 D. S. Mu, T. B. S. V. Naga Lakshmi, D. Kumaresan, R. Krishna Prasad and M. Sivakumar, Hydrothermal synthesis, phase control, and dielectric analysis of niobium-doped barium strontium titanate, *J. Mater. Sci.: Mater. Electron.*, 2025, **36**, 820.

25 K. G. Baiju, A. Nagarajan, A. M. G. Sadasivam, D. D. S. Rajan, S. S. Vignathi, M. Balu and D. Kumaresan, Hydrothermal synthesis, dielectric properties of barium titanate, cobalt-doped barium titanate, and their graphene nanoplatelet composite, *Asia-Pac. J. Chem. Eng.*, 2020, **15**(5), e2550.

26 M. Balu, K. G. Baiju, R. K. Prasad and D. Kumaresan, Fabrication of Barium Titanate Nanowires-GNP Composite Bilayer Photoanodes for the High-Performance Dye-Sensitized Solar Cells, *Appl. Surf. Sci.*, 2023, **610**, 155316.

27 N. Ma and Y. Yang, Boosted photocurrent in ferroelectric BaTiO3 materials via two-dimensional planar-structured contact configurations, *Nano Energy*, 2018, **50**, 417.

28 W. Qian, H. Wu and Y. Yang, Ferroelectric $BaTiO_3$-Based Multi-Effects Coupled Materials and Devices, *Adv. Electron. Mater.*, 2022, **8**, 2200190.

29 Y. Jiang, F. Li, X. Li, W. Fang, X. Si, T. Zhou, Y. Min and Y. Liu, Study on the charge carrier transport property generated by photo/piezo synergy field over barium strontium titanate, *Nano Energy*, 2023, **114**, 108600.

30 L. Y. Chiu and K. S. Chang, Textured $BaTiO_3$ nanorod arrays synthesized via hydrothermal method: Enhanced degradation of Rhodamine B with piezocatalysis, *Ceram. Int.*, 2025, **51**, 29167.

31 M. Qamar, S. A. Zaidi, M. Rafatullah, M. Qutob, S. J. Kim and Q. A. Drmosh, Role of Post-Hydrothermal Treatment on the Microstructures and Photocatalytic Activity of TiO_2-Based Nanotubes, *Catalysts*, 2022, **12**(7), 702.

32 Y. Xu, X. Fang, J. Xiong and Z. Zhang, Hydrothermal transformation of titanate nanotubes into single-crystalline TiO_2 nanomaterials with controlled phase composition and morphology, *Mater. Res. Bull.*, 2010, **45**, 799.

33 V. Etacheri, Y. Kuo, A. Van der Ven and B. M. Bartlett, Mesoporous TiO_2–B microflowers composed of (1 −1 0) facet-exposed nanosheets for fast reversible lithium-ion storage, *J. Mater. Chem. A*, 2013, **39**, 12028.

34 R. Ye, Z. Wang and Y. Xue, *et al.*, Effect of raw material concentration on the morphology of nano-barium titanate ribbon-like fibers synthesized by hydrothermal, *J. Mater. Sci.:Mater. Electron.*, 2024, **35**, 1750.

35 Z. Deng, Y. Dai, W. Chen, X. Pei and J. Liao, Synthesis and Characterization of Bowl-Like Single-Crystalline $BaTiO_3$ Nanoparticles, *Nanoscale Res. Lett.*, 2010, **5**, 1217.

36 L. Liang, X. Li, Y. Sun, Y. Tan, X. Jiao, H. Ju, Z. Qi, J. Zhu and Y. Xie, Infrared Light-Driven CO_2 Overall Splitting at Room Temperature, *Joule*, 2018, **2**, 1004.

37 I. C. Maurya, S. Senapati, S. Singh, P. Srivastava, P. Maiti and L. Bahadur, Effect of Particle Size on the Performance of TiO2-Based Dye-Sensitized Solar Cells, *ChemistrySelect*, 2018, **3**(34), 9872.

38 H. Lemziouka, F. Nekkach, A. Boutahar, R. Moubah, L. H. Omari, M. Filali, A. Rjeb, H. Lassri, M. Abid, E. K. Hlil and M. E. Yazidi, Effect of Cobalt Doping on the Structural, Linear, and Nonlinear Optical Properties in $Ba_{1-x}Co_xTiO_3$ Perovskites, *J. Electron. Mater.*, 2023, **52**, 3420.

39 N. N. Hasbullah, S. K. Chen, K. B. Tan, Z. A. Talib, J. Y. C. Liew and O. J. Lee, Photoluminescence activity of BaTiO3 nanocubes via facile hydrothermal synthesis, *J. Mater. Sci.: Mater. Electron.*, 2019, **30**, 5149.

40 G. Thorner, J. M. Kiat, C. Bogicevic and I. Kornev, Axial hypertoroidal moment in a ferroelectric nanotorus: A way to switch local polarization, *Phys. Rev. B: Condens. Matter Mater. Phys.*, 2014, **89**, 220103.

41 T. Charoonsuk, S. Sriphan, C. Nawanil, N. Chanlek and W. Vittayakorn, Tetragonal $BaTiO_3$ nanowires: A template-free salt-flux-assisted synthesis and its piezoelectric response based on mechanical energy harvesting, *J. Mater. Chem. C*, 2019, **7**, 8277.

42 W. W. Lee, W. H. Chung, W. S. Huang, W. C. Lin, W. Y. Lin, Y. R. Jiang and C. C. Chen, Photocatalytic activity and mechanism of nano-cubic barium titanate prepared by a hydrothermal method, *J. Taiwan Inst. Chem. Eng.*, 2013, **44**, 660.

43 R. X. Wang, Q. Zhu, W. S. Wang, C. M. Fan and A. W. Xu, $BaTiO_3$–graphene nanocomposites: synthesis and visible light photocatalytic activity, *New J. Chem.*, 2015, **39**(6), 4407.
44 C. Y. Wei, S. H. Kuo, Y. M. Hung, W. C. Huang, F. Adriyanto and Y. H. Wang, High-Mobility Pentacene-Based Thin-Film Transistors with a Solution-Processed Barium Titanate Insulator, *IEEE Electron Device Lett.*, 2011, **32**, 90.
45 S. Fuentes, H. Pizarro, P. Gutiérrez, D. E. Diaz-Droguett and N. Barraza, Application of FORC distributions to the study of magnetic interactions in Co-doped $BaTiO_3$ nanomaterials, *Mater. Sci. Eng. B*, 2018, **227**, 39.
46 N. Farahmand, C. K. McGinn, Q. Zhang, Z. Gai, I. KKymissis and S. O'Brien, Magnetic and dielectric property control in the multivalent nanoscale perovskite Eu0.5Ba0.5TiO3, *Nanoscale*, 2021, **13**, 10365.
47 E. A. Gibson, L. L. Pleux, J. Fortage, Y. Pellegrin, E. Blart, F. Odobel, A. Hagfeldt and G. Boschloo, Rethinking the Role of the Electrolyte in p-Type Dye-Sensitized Solar Cells: A Comparative Study of the Iodide/Triiodide and Cobalt(II)/(III) Redox Mediators Combined with the P1 Sensitizer, *Langmuir*, 2012, **28**(15), 6485.
48 C. Cavallo, F. D. Pascasio, A. Latini, M. Bonomo and D. Dini, Nanostructured Semiconductor Materials for Dye-Sensitized Solar Cells, *J. Nanomater.*, 2017, 5323164.
49 L. W. Qing, L. G. Guan, K. D. Xing, H. L. Hua and D. S. Yuan, Wide frequency range diagnostic impedance behavior of the multiple interfaces charge transport and transfer processes in dye-sensitized solar cells, *Electrochim. Acta*, 2013, **88**, 395.
50 K. Park, Q. Zhang, D. Myers and G. Cao, Charge Transport Properties in TiO2 Network with Different Particle Sizes for Dye Sensitized Solar Cells, *ACS Appl. Mater. Interfaces*, 2013, **5**, 1044.
51 M. Pazoki, U. B. Cappel, E. M. J. Johansson, A. Hagfeldt and G. Boschloo, Characterization techniques for dye-sensitized solar cells, *Energy Environ. Sci.*, 2017, **10**, 672–709.
52 L. Tao, Z. Huo, Y. Ding, Y. Li, S. Dai, L. Wang, J. Zhu, X. Pan, B. Zhang, J. Yao and M. K. Nazeeruddin, High-efficiency and stable quasi-solid-state dye-sensitized solar cell based on low molecular mass organogelator electrolyte, *J. Mater. Chem. A*, 2015, **3**(5), 2344.
53 J. K. Li, C. Ge, K. J. Jin, J. Y. Du, J. T. Yang, H. B. Lu and G. Z. Yang, Self-driven visible-blind photodetector based on ferroelectric perovskite oxides, *Appl. Phys. Lett.*, 2017, **110**(14), 142901.
54 D. K. Bhat, H. Bantawal and U. S. Shenoy, Rhodium doping augments photocatalytic activity of barium titanate: effect of electronic structure engineering, *Nanoscale Adv.*, 2020, **2**(12), 5688–5698.
55 R. X. Wang, Q. Zhu, W. S. Wang, C. M. Fan and A. W. Xu, $BaTiO_3$–graphene nanocomposites: synthesis and visible light photocatalytic activity, *New J. Chem.*, 2015, **39**(6), 4407.
56 S. Xu, Z. Liu, M. Zhang and L. Guo, Piezotronics enhanced photocatalytic activities of Ag-$BaTiO_3$ plasmonic photocatalysts, *J. Alloys Compd.*, 2019, **801**, 483.
57 I. K. Biernacka, B. G. Glos, E. Skiba, W. Maniukiewicz, W. Bąk, M. Antonova, S. Rebelo and C. Freire, Evaluation of Rhodamine B photocatalytic degradation over $BaTiO_3$–MnO_2 ceramic materials, *Materials*, 2021, **14**, 3152.